Synoptic density and velocity observations of slope waters in the Chukchi and East-Siberian Seas

Andreas Münchow

Institute of Marine and Coastal Sciences
Rutgers, The State University of New Jersey
71 Dudley Rd.
New Brunswick, NJ 08901-8521
U.S.A.

Eddy C. Carmack

Institute of Ocean Sciences
Sidney, British Columbia
Canada

David A. Huntley

Institute of Marine and Coastal Sciences
Rutgers, The State University of New Jersey
New Brunswick, New Jersey
U.S.A.

Re-Submitted to J. Geophys. Res.

January 2000

1. Abstract

Synoptic velocity and water mass observations obtained in 1993 provide a snapshot of the circulation over the slope of the Chukchi and East Siberian Seas. We describe flow and density fields between the 100-m and 2000-m isobaths more than 350 km to the north of Siberia near the Date Line. Strong property gradients on sloping isopycnal surfaces reflect sharp boundaries between upper and lower halocline, as well as Atlantic layer waters. Concurrent velocity observations from a towed acoustic Doppler current profiler reveal an unexpected, 5-10 cm/s strong generally westward subsurface flow between the 200-m and 350-m isobaths. The flow is most intense 50-m to 150-m below the surface and is embedded in a tidal currents with amplitudes of similar magnitude. Subtidal velocity and water mass observations from sections 250 km apart suggest a spatially continuous westward slope current. Variability associated with sub-mesoscale vortices is shown by a geostrophically-balanced anti-cyclonic eddy which carries anomalous warm shelf water of Pacific origin. The eddy is nearly spun-down: its Rossby number of about 0.1 is an order of magnitude smaller than those of eddies observed in the Beaufort Sea.

2. Introduction

After the conclusion of the Russian Civil War in 1922, a young Norwegian oceanographer set out from eastern Siberia to cross the deep Arctic Ocean from the Pacific to the Atlantic. His ship the *Maud* failed, however, to leave the vast continental shelves of the Chukchi and East Siberian Seas. Harald Sverdrup meticulously collected and thoroughly analyzed velocity and hydrographic data that still form the most complete and accessible description of the North-Siberian waters (Sverdrup, 1929). After the dissolution of the Soviet Union, the Canadian Coast Guard Ship *Henry Larsen* was denied entry into these waters

in 1993 and thus operated in waters north of the 200 nm Russian Exclusive Economic Zone. We report velocity and density observations from this unique opportunity to survey the waters over the continental slopes to the north of Eastern Siberia and Alaska.

Intense current systems generally occur where the deep ocean adjoins shallow shelves. Continental slopes “trap” kinetic energy and currents advect waters generally in the direction of Kelvin wave propagation. The “trapping” of kinetic energy is the result of the earth’s rotation that dynamically constraints flows over topographic features since vortex tube stretching or squashing is much enhanced near topographic slopes (Huthnance, 1992, 1995). More specifically, small across-slope pertubations propagate cyclonically along the slope, cause oscillations downstream near the slope, and thus “trap” kinetic energy of both shelf and basin circulation. Subsurface slope currents are found off California (Huyer et al., 1989), Oregon (Collins et al., 1996), Peru and Chile (Fonseca, 1989), as well as in the Arctic Ocean (Aagaard, 1984; Treshnikov, 1977). They generally oppose the broader wind-driven surface circulation.

In the Arctic Ocean the eastward flowing Beaufort Undercurrent constitutes the most prominent boundary current (Aagaard, 1984). It opposes the wind-driven surface circulation over the Canada Basin and is partly fed by Pacific waters entering the Arctic Ocean through Bering Strait (Coachman and Aagaard, 1988). These Pacific waters supply the partly buoyancy driven Alaska Coastal Current which flows along the Chukchi shelf until it enters the Beaufort Sea through Barrow Canyon (Paquette and Bourke, 1974; Münchow and Carmack, 1997). It then supplies the Beaufort Undercurrent with anomalously warm water in the summer (Aagaard, 1984). The generally upwelling favorable (anti-cyclonic) winds over the Beaufort Sea force the Beaufort gyre which constitutes the main surface

circulation feature over the Canada Basin. The Beaufort Undercurrent opposes this geostrophically balanced surface current over the narrow continental slope at depth. From these prior findings we expect a similar subsurface slope current to circulate waters "cyclonically" (eastward) over the slope of the East Siberian and Chukchi slope seas. We will find, however, an "anti-cyclonic" (westward) circulation over the continental slope of the Chukchi and East Siberian Seas at depth.

The waters of the western Arctic Ocean are populated by sub-mesoscale vortices embedded in the halocline layer (e.g., Newton et al., 1974; Manley and Hunkins, 1985; D'Asaro, 1988a; and Plueddemann et al., 1998). Their anomalous water mass properties implicate generation regions on or near continental shelves. It is still unclear, however, exactly where, when, and how these eddies form. D'Asaro (1988b) proposed that lateral friction and flow separation near the bending coastline off Barrow explains the abundant eddies in the Beaufort Sea, however, direct velocity observations have yet to detect eddy formation. Stern and Whitehead (1990) as well as Klinger (1994) conducted laboratory studies that successfully simulated eddy formation near a bending coastline, however, a realistic numerical process study of the shelf/slope region near Barrow failed to simulate eddy formation (Signorini et al., 1997). The same numerical model explained limited velocity observations rather well. It is thus not yet possible to conclusively explain formation and characteristics of the abundant sub-mesoscale vortices in the Arctic Ocean.

Analyzing 1993-1994 hydrographic and tracer data, Carmack et al. (1995), McLaughlin et al. (1996), and Macdonald (1996) report that Atlantic waters displaced Pacific waters in the upper 200-m from the Lomonosov to the Mendeleyev Ridge during the last decade. Regions of enhanced gradients were discovered and termed "fronts" (McLaughlin et al.,

1996). Smith et al. (1999) find similar “fronts” at similar location in the 1995-1996 distribution of tracers released from nuclear fuel reprocessing plants in Sellafield, UK and La Hague, France. The above studies describe the large basin-scale tracer and water mass distributions from widely spaced stations that emphasize variability in the Canada and Makarov Basins along the slope near the 2000 m isobath. In contrast, we here focus on this “frontal” scale by examining more closely spaced CTD and ADCP data from shipborne surveys that resolve the internal deformation radius in the summer of 1993. Furthermore, we emphasize variability across the continental slope of the water column above 500-m.

3. Study area and data sources

Figure 1 shows the Western Arctic along with three across-slope survey lines that the *CCGS Henry Larsen* occupied in the summer of 1993. No surface vessel had previously entered this area between 170°W and 170°E longitude more than 200 nm to the north of Russian territory. Nevertheless, an exceptionally light ice year facilitated an extensive sampling program that included detailed hydro-cast (McLaughlin et al., 1996) and fast synoptic surveys (Münchow and Carmack, 1997). The synoptic surveys used a self-contained SeaBird SEACAT CTD with an external pump to ensure good flushing of the conductivity cell. This CTD was calibrated and compared against bottle, Guildline, and Falmouth Scientific Integrated CTD data; McLaughlin et al. (1996) detail calibration and processing of all hydrographic data collected during the 6-week cruise.

An acoustic Doppler current profiler (ADCP) tow system was deployed as time and ice conditions permitted. Münchow et al. (1995) describe the system, its performance, as well

as details of the data calibration and processing. Briefly, the tow system included a downward profiling 153 kHz NarrowBand ADCP of RDI Inc. housed inside an ENDECO V-fin tow body, a 7-conductor load-carrying cable for real-time communication with the ADCP, and an upward profiling 614 kHz ADCP. The system was towed about 15-m below the surface alongside the bow of the ice breaker. The velocity data were collected in beam coordinates with 4 pings per ensemble in 8-m vertical bins, screened, calibrated, and only then averaged into 10 minute temporal averages. The 10 minute data were then again screened thoroughly for changes in ship speed and direction as well as quality control parameters (Münchow et al., 1995).

The subsurface tow uses a magnetic compass that, at high latitudes and near the steel hull of an ice breaker, is severely biased. A local compass calibration is thus essential to ensure data quality (Münchow et al., 1995). **Figure 2** shows a comparison of the ship's absolute velocity over the ground as determined from navigational GPS data and the bottom tracking pings of the ADCP after all calibrations; the two independent velocity estimates agree reasonably well. Discrepancies are caused by both inaccurate compass and navigational data. The ADCP always tracks the bottom and errors common to both water and bottom tracking pulses are minimized since earth referenced velocities are the difference of velocities derived from bottom and water tracking pulses. The averaged velocity over 60 ensembles (each with 4 pings/ensemble) over 5-10 minutes results in a random velocity error of less than 1 cm/s, however, this uncertainty of the actual measurement is small relative to the bias introduced by physical processes such as internal waves and tidal currents remnants of which, using the best available detiding algorithms can exceed 3 cm/s (Münchow, 2000). The calibration coefficients and accuracies over the slope of the Chukchi and East

Siberian Seas are different from those near Barrow (Münchow and Carmack, 1997) because the earth's magnetic field changes rapidly in space at high latitudes. We here claim accuracies in compass and thus absolute current direction of about 6°.

4. Hydrography

McLaughlin et al. (1996) introduce the concept of "water mass assembly" in order to discuss changes in the oceanography of the Arctic Ocean. They distinguish between an Eastern and a Western Arctic assembly of distinctly layered water masses and term the boundary between these assemblies the Atlantic/Pacific front. The main difference between these two assemblies is the large fraction of relatively fresh, warm, and silicate rich halocline waters in the Western Arctic assembly. Using hydro-cast data from stations seaward of the 2000-m isobath only (e.g., the most offshore stations on sections C, D, and E shown in Figure 1), McLaughlin et al. (1996) report a spatial shift of the boundary between these assemblies from the Lomonosov Ridge at 140°E to the Mendeleyev Ridge at 180°. While the "assemblies" extend to water masses below the 2000-m deep sill depth of the Lomonosov Ridge, we discuss variability only in the upper 500-m of the water column where the changes are most pronounced. After a brief discussion of water mass properties at select stations, we present the spatial distribution of properties on isopycnal surfaces and across-slope sections.

Figure 3 shows temperature-salinity correlations for seven select stations. Halocline waters with salinity between 33.0 and 34.5 show a large spread in temperature from more than -1.0 °C in the east (open circles in Figure 3) to less -1.6 °C in the west (filled rectangles in Figure 3). A large fraction of this spread takes place at scales of less than 50 km,

since waters in the triangular study area (Figure 1b) contain waters of both Pacific (open triangles in Figure 3; station TA) and East Siberian influence (open rectangles in Figure 3; station TC). Data from station T8 fluctuate between these extremes as evidenced by a 40-m thick “warm” intrusion near the σ_θ=26.9 isopycnal (filled circles in Figure 3). Hence substantial variability and isopycnal mixing occur within our study area.

A second distinct difference in the two assemblies is the depth at which subsurface temperature maxima occur. A shallow temperature maximum near salinity 32.0 is often associated with the presence of Bering Sea Summer waters (Coachman and Barnes, 1961). Drifting with the pack ice from 1922-24 along the 60-m isobath of the western Chukchi and East Siberian Shelf Seas, Sverdrup (1929) observed a small but distinct temperature maximum at the higher salinity of 32.6 near the σ_θ=26.3 isopycnal. For the stations on the slope of the triangular study area (e.g., stations TA, TC, T8, and T15), we find a similar temperature maximum near this isopycnal. **Figures 4**a and 4b show the potential temperature and pressure, respectively, on this isopycnal for the entire study area. The temperature maximum of -1.3 °C about 70-m below the surface is centered on the triangle (Figures 4a and 4b) suggesting, we believe, a lateral injection of Bering Sea waters. In contrast, we find cooler waters of nearly -1.6 °C on this isopycnal both to the west and to the east. We propose that these “warmer” waters reached the triangle from the inner shelves off Siberia through Hope Valley. Furthermore, in section 5 we will demonstrate that this transport of warmer water occurs in the form of an anti-cyclonic eddy embedded within the halocline.

Deeper down we find the σ_θ=27.5 isopycnal at 100-m depth in the East Siberian Sea and at 180-m depth in Chukchi Sea (Figures 4d). This isopycnal represents cold lower halocline waters that reflect the cooling influence of brines advected across the shelves and

slopes (Aagaard et al., 1981). They overlie the warm Atlantic layer waters below and insulate the ice cover from this source of heat. The waters constituting the σ_θ=27.5 isopycnal have temperatures of less than -1.4 °C in the western part of our study area that includes the Mendeleyev Ridge. In the eastern part of our study area temperatures vary from -1.4 °C to -0.9 °C (Figure 4c). The largest isopycnal temperature gradients of about 0.003 °C/km occur within the triangle. Within this area the σ_θ=27.5 isopycnal is almost flat at 130-m depth (Figure 4d). Largest isopycnal slopes occur along section C in the east where the halocline tilts upward towards the shelf from 180-m offshore to less than 110-m inshore. The situation is reminiscent of the Beaufort gyre where Münchow and Carmack (1997) find similarly enhanced isopycnal slopes especially near Barrow Canyon. It thus appears conceivable that the halocline layer at section C extends into the western limb of the wind-driven, anti-cyclonic Beaufort gyre. In section 6 below we will demonstrate, however, that unlike the surface intensified Beaufort gyre, the tilting isopycnals of section C are not compensated by a flow in thermal wind balance.

Deeper down yet, we find Atlantic core waters (σ_θ=27.9; Figures 4e and 4f) with temperatures between +0.2 °C and +1.2 °C (Figure 4e). Temperatures less than +0.4 °C occur over the slope of both the eastern and western Chukchi Sea sections C and D, respectively. In contrast, the waters on the same isopycnal over the slope of the East Siberian Sea exceed +1.2 °C. Unlike the isopycnal temperature gradients of the upper and lower halocline waters, the largest temperature gradient of the Atlantic core waters coincide with the location of the Mendeleyev Ridge (Figure 4e). McLaughlin et al. (1996) identify these waters as recently ventilated Atlantic waters using a suite of geochemical tracers. Similar to the halocline σ_θ=(26.3, 27.5), the deep isopycnal is almost flat (at 270-m) in the area of largest

temperature gradients. In contrast to the halocline, however, across-slope isopycnal slopes are relatively small everywhere. Nevertheless, the core of the Atlantic layer is 40-m deeper at section C in the east than it is at section E in the west (Figure 4f).

The delicate three-dimensional arrangement of the density field above 500-m depth becomes particularly clear in **Figure 5**. It shows three across-slope sections of the potential density below the surface mixed layer. Vertical density gradients below 100-m depth increase from section E to section C. The vertical extent of the surface layer with σ_θ<26.2 deepens from about 40±10 m at section E (Figure 5a) to about 100±20 m at section C (Figure 5c). Note that the σ_θ=26.2 isopycnal is almost flat across both sections E and D. In contrast, it slopes across section C from about 60 m inshore to 100 m offshore. The ocean was ice-free shoreward of the 200-m isobath. Wind-forced motions thus could affect the density field through Ekman flux convergence and divergence within surface and bottom boundary layers. We also find upward sloping isopycnals shoreward of the 700-m isobath at section D which, if balanced geostrophically, implies a westward near surface flow relative to no flow at depth.

5. The East Siberian slope region

Using one of the earliest current meters available, Sverdrup (1926) reported measurements of tidal currents at several locations during his 2-year long drift along the shelves off Siberia. From such detailed current and additional sea level observations he concluded on dynamical grounds, that no large land mass could exist in the Arctic Ocean (Sverdrup, 1926). He also found M_2 tidal currents of about 20 cm/s, 15 cm/s, and 7 cm/s at stations #2, #3, and #4 (see Figure 1 for locations) to rotate clockwise on an ellipse with a ratio

between minor to major axis of about 0.8-0.9. Tidal currents were strongly baroclinic with the largest amplitude at the location of the pycnocline. These observations constitute the only measurements against which we can compare our velocity measurements. The horizontal velocity estimates from the ADCP shown in Figure 6 are of the same order of magnitude as the tidal currents reported by Sverdrup (1926) 200 km to the south-west, i.e., it is likely that tidal currents substantially bias velocity survey data over the outer shelf and slope regions of the western Chukchi and East Siberian Seas. It is therefore necessary to estimate tidal currents from our ADCP records in order to minimize the tidal bias in our observations. Our detiding methodology closely follows prior work by Candela et al. (1993), Münchow et al. (1993), and Münchow (2000). The appendix details the method and error estimates.

The velocity survey around the triangle consisted of continuously profiling along the base of the triangle from stations TA to TB and discrete station work along the two offshore sections from TB to TC and from TC to TA (Figure 1b). The shelf break is steeply sloping as the depth increases by 80-m in 10 km. It took almost 20 hours to complete the survey that included 19 CTD casts at about 7 km station spacing. **Figure 6** shows the data set as a scatter plot of all vertical velocity profiles around the perimeter of the triangle. Velocity profiles extend to about 250-m to 300-m depth where the velocity is close to zero. Vertical shear is substantial in the upper 100-m of the water column especially where maximum westward velocities reach 25 cm/s. Error velocities are generally smaller than 1 cm/s indicating that the vertical velocity estimates from beams 1 and 2 are very close to the vertical velocity estimate from beams 3 and 4. Actual vertical velocities are shown only as indicators of data quality and no other meaning is attached to them.

Figure 7 maps detided current vectors along with the density anomaly σ_θ at selected depths. The most striking feature is an apparent anti-cyclonic eddy in the south-east corner of the triangle near TA and a generally westward flow along the base of the triangle between TA and TB (Figure 7). Both features appear strongest at 100-m depth (Figure 7b) and diminish both towards the surface (Figure 7a) and the bottom (Figure 7c). The sloping isopycnals at 60-m and 100-m are qualitatively consistent with an anti-cyclonic circulation in thermal wind balance that has a subsurface velocity maximum. More specifically, waters at the center of the eddy at 60-m depth are denser than surrounding waters while those at 100-m depth are lighter than surrounding waters. Isopycnals thus dome upward towards the center at 60-m depth while they dome downward towards the center at 100-m depth. This arrangement is characteristic of anti-cyclonic eddies with a subsurface velocity maximum near the main pycnocline (D'Asaro, 1988a; Manley and Hunkins, 1985). The circulation at 140-m depth (Figure 7c) and below (not shown) is weak. We thus conclude that the most energetic circulation takes place within the local temperature maximum layer with densities near σ_θ=26.2 (Figures 3 and 4a) and diminishes deeper within the halocline layer (Figures 3 and 4b). The presence of the eddy near stations TA and T15 may also explain the scatter in the water mass properties in the halocline (Figure 3), i.e., waters on isopycnals in the range σ_θ=(26.3, 27.3) are about 0.2 °C warmer than they are offshore at TC and beyond (Figures 3 and 4). The cause for this scatter thus is the injection of warmer shelf waters in the form of eddies.

The distribution of both the westward and northward flow component along the base of the triangle becomes particularly clear in **Figure 8**. The zonal flow is to the west at all depths and approaches zero near the bottom (Figure 8a). The meridional flow is to the north in the

upper 150-m of the water column (Figure 8b). A small southward velocity component of about 2 cm/s is barely visible between 150-m and 200-m depth, it diminishes toward zero below 200-m depth. The net volume flux normal to this east-west section is 0.04 Sv to the north (1 Sv=10^{-6} m^3/s), however, this estimate is not significantly different from zero considering uncertainties of about 2 cm/s in both the absolute velocity estimation from the ADCP and the estimation of tidal currents. Nevertheless, the subsurface velocity maximum of about 10 cm/s to the west and 6 cm/s to the north is quite robust and occurs at 75-m depth. We note that the flow near the corner of the triangle at TA has a southward component that reaches 6 cm/s, i.e., this flow component changes from -6 cm/s to +6 cm/s within less than 10 km. Taking this horizontal velocity difference δv=12 cm/s over the distance δx=10 km as an estimate of the relative vorticity ξ, we find

$$\xi = \frac{\partial v}{\partial x} - \frac{\partial u}{\partial y} \approx \frac{\delta v}{\delta x} = \frac{-0.12m}{10km} \cong -0.09 \cdot f \qquad (1)$$

where $f=1.4\times10^{-4}\ s^{-1}$ is the Coriolis parameter (planetary vorticity) at 75°N. The ratio between relative and planetary vorticity constitutes a Rossby number (Pedlosky, 1986) that scales the nonlinear inertial acceleration in the momentum balance. The ratio $\xi/f=O(0.1)$ here is small, the abundant eddies in the Beaufort Sea reported by D'Asaro (1988a) frequently have ξ/f=O(1). We thus suggest that the observed eddy is quite old with much of its kinetic energy already dissipated.

Curiously, though, the isopycnals along the base of the triangle are flat (not shown). The 7 km spacing of the CTD stations thus does not properly resolve the density field associated with the eddy. In contrast, the density section from TC to TA does show doming isopycnals (**Figure 9**a) suggestive of an anti-cyclonic flow in geostrophic balance. If the baro-

clinic pressure gradient associated with this density distribution is indeed geostrophically balanced, then we can estimate the velocity distribution from the density field through the thermal wind relation, e.g.,

$$\frac{\partial v}{\partial z} = \frac{1}{f \cdot \rho_0} \cdot \frac{\partial \rho}{\partial x} \qquad (2)$$

which gives, relative to no-flow at 275-m, the geostrophic velocity field shown in Figure 9b; here v is the velocity component normal to the density sections, f is the Coriolis parameter, and ρ_0 is a reference density. The geostrophic flow is generally weak (<2 cm/s), except at 90-m depth near TA at the south-eastern corner of the triangle. There a 4 cm/s flow out of the triangle is adjacent to a 10 cm/s flow into the triangle. The lateral velocity difference of the geostrophic flow at this depth is thus about 14 cm/s over 15 km (Figure 9b) which is very similar to what is observed along the base of the triangle (Figure 8). The direct comparison between thermal wind velocity and ADCP current observations at 90-m depth shows fair agreement (Figure 9c). Large discrepancies occur to the south-east of station TC where we observe a flow 5 cm/s into the triangle while the thermal wind velocity is close to zero. We suspect that both the detiding method and noise in the ADCP currents contribute to these discrepancies. Nevertheless, velocity magnitude, direction, and lateral current shear associated with the eddy are explained well by the thermal wind relation.

In summary, the flow over the slope of the western Chukchi Sea 350 km to the north of Wrangel Island is weak (<5 cm/s) with a subtidal component to the north-west. Larger velocities occur at tidal time scales and during the passage of a sub-mesoscale vortex. The observed vortex is both weak (ξ/f=O(0.1)) and in thermal wind balance. Its location coin-

cides with a region of strong isopycnal property gradients and associated scatter of water mass properties (Figures 3 and 4).

6. The Chukchi slope region

The ADCP/CTD survey of the eastern Chukchi slope region covers the upper slope from the 80-m to the 200-m isobath (Figure 1c). Here the shelf break slopes gently by about 20-m in 10 km. The data from the 30 hour survey consist of 7 discrete CTD stations and continuous ADCP profiling at ship speeds of about 4 m/s. Data processing is identical to that outlined above, the same calibration and screening coefficients are applied to this region east of the triangle. We know little about the tidal currents in this region. Sverdrup (1926) reports data from a survey in Herald Canyon adjacent to Wrangel Island where tidal currents reach 16 cm/s at the surface. In contrast, near Barrow tidal currents are less than 2 cm/s (Mountain et al., 1976; Kowalik and Proshutinsky, 1994). Again we use ADCP velocity observations to estimate tidal currents using methods detailed in the appendix.

Figure 10 indicates that the subtidal circulation at depths above 100-m is to the east in the same general direction as the weak (< 5 m/s) winds (not shown), however, below this depth and especially offshore the flow is in the opposite direction, i.e., to the west. This spatial arrangement of currents is best visualized in **Figure 11** that shows along- and across-slope velocity components of an across-slope section. Flow structures indicate a surprising amount of spatial variability at horizontal scales of about 25 km. Inshore of the 100-m isobath the flow is almost uniformly to the east with an onshore component. Smallest along-slope velocities occur between the 100-m and 150-m isobath while further offshore the flow intensifies and reverses its direction from eastward to westward at depth.

Offshore the near surface flow is convergent and to the east while the near bottom is divergent and to the west (Figure 11a). If the implied vertical, i.e., downward flow takes place, then we expect a locally depressed pycnocline. Figures 4b, 4d, and 5c indeed indicate isopycnals along this section C that are deeper in the water column than elsewhere. If the westward flow near the bottom (Figures 10c and 11a) is continuous along the Chukchi slope, then it can explain the strong similarity of halocline waters at this location ("+" symbol in Figure 3) with those 250 km to the west at TA ("Δ" symbol in Figure 3; see also Figure 1 for locations). We thus propose that the observed westward flow at about 100-m to 150-m depth is continuous along the Chukchi slope seaward of the 200-m but shoreward of the 400-m isobath. Measurements of longer duration than the daily snapshots provided here are needed to confirm or dispute this unexpected westward flow of halocline waters along the upper Chukchi slope.

7. Conclusions

The hydrographic conditions observed in 1993 over the slope of the Chukchi Sea suggest substantial horizontal variability in both Pacific and Atlantic water masses. Building on the findings of McLaughlin et al. (1996), we here focus on the density and velocity fields at scales that resolve the internal deformation radius. The "frontal" feature that separates "eastern" and "western" Arctic water mass assemblies defined by McLaughlin et al. (1996) penetrates beyond the Mendeleyev Ridge into the Chukchi borderland. Furthermore, water mass boundaries on along-slope sloping isopycnals occur at scales smaller than 25 km.

In the Chukchi Sea intensified flows occur inshore of the 500-m isobath. Baroclinic processes that involve eddies as well as delicately arranged convergent and divergent flow field patterns appear that are embedded in tidal currents with amplitudes up to 10 cm/s. An anti-cyclonic eddy in approximate thermal wind balance is observed near the previously reported water mass boundary. Unlike the eddies reported from the Beaufort Sea, however, the anti-cyclonic Chukchi slope eddy is very sluggish with a Rossby number of O(0.1). It is probably in the final stage of spin-down after, we speculate, a long path from a generation region to the south-east. This specific eddy appears to drift with the ambient, generally westward flow along the slope.

The generally westward flow above 300-m depth along the upper slope surprises and is contrary to dynamical expectations as subsurface slope currents in the Arctic and elsewhere generally flow in the direction of Kelvin wave propagation. It is also contrary to many schematic flow representations that are drawn for this data sparse region, e.g., Rudels et al. (1995) and McLaughlin et al. (1996). We note, however, that the direct flow field observations reported here are very short snapshots. Nevertheless, the same westward flow emerges from 2 areas separated in space and time by 250 km and 10 days, respectively. It thus is possible that the westward flow over the Chukchi slope is not an isolated, daily feature. Furthermore, it appears conceivable that the narrow Arctic boundary currents bypass the broad and gently sloping area to the south of the Chukchi Plateau. We thus speculate on a partly closed circulation loop around the Chukchi Plateau with northward flow to the east, eastward flow to the north, southward flow to the west, and westward flow to the south of the plateau. Moored instrumentation to the west of Barrow

Canyon and east of the Chukchi Plateau are necessary to establish the direction and intensity of the flow over the Chukchi slope.

The exact forcing of both the observed flow and the shifting water mass boundaries are still unclear and cannot be addressed with the data presented here. The winds over the region during the period of our observations were weak, generally less than 5 m/s, however, a persistent wind stress curl may contribute to the circulation in this region. A comprehensive review of the wind field at daily to decadal time scales is underway using the TOVS data sets (Francis et al., 1999). Pressure gradient forces imposed by the steric sea level difference between the Pacific and Arctic Oceans (Stigebrandt, 1984), too, almost certainly impact the circulation along the Chukchi slope at monthly, seasonal, and inter annual time scales. At the much shorter, daily time scale, however, we expect topographic vorticity waves to propagate through the area, interact with spatially variable buoyancy fluxes, and/or scatter kinetic energy into smaller scale motions and eddies (Yankovsky and Chapman, 1997). An investigation of any of these forcing processes requires a carefully designed mooring array that consists of both current meters, pressure sensors, and strings of temperature and conductivity sensors.

8. Acknowledgements

The 1993 field work would not have been possible without the support of Nan Bray, Myrl Hendershott, and Clinton Winant of Scripps Institution of Oceanography (SIO). They gave crucial advice, encouragement, and instrumental support. The generous loan of the towed ADCP system at is just one of many examples. Aboard the *CCGS Henry Larsen*, Captain Gomes and his superb crew including the bosun Claude Robilard ensured safe and innova-

tive deployment of all instrumentation. Doug Sieberg and Rick Pearson of the Canadian Institute of Ocean Sciences as well as Charly Coughran of SIO and Dyrl Simons of RDI Inc. were instrumental with the many technical details that accompany all field work. Robie Macdonald was a fine and generous Chief Scientist during the 6-week expedition. Constructive comments by three anonymous reviewers improved the manuscript. The data collection was supported by Tom Curtin of the Office of Naval Research (ONR) through grant N00014-94-0041 while the data processing and analysis was supported by ONR grant N00014-95-1-1157 as part of the Arctic Nuclear Waste Assessment Program.

9. Appendix: Tidal currents

Tidal currents constitute a quasi-periodic signal that generally biases velocity observations from a moving ship. While tidal sea level observations generally vary smoothly over large spatial areas away from small coastal embayments, tidal currents often reveal spatial and temporal variations not always accounted for by sea level oscillations (Münchow, 1998). Direct velocity observations from current meter moorings in the Arctic are rare. Furthermore, available records can not always be extrapolated in time and space. We here outline our methods to reduce the tidal bias and to estimate errors in the estimation of tidal currents.

9.1 Tidal currents over the East Siberian slope

Guided by prior observations (Sverdrup, 1926) and experience in detiding ADCP survey data (Candela et al., 1992; Münchow et al., 1992b; Münchow, 2000), we assume that the tidal currents (u_T,v_T) in the triangular study area (Figure 1b) consist of a single semi-diurnal M_2 constituent with a frequency $\omega=2\pi/T$ (T=12.42 hours) that varies in the vertical z

but not in the horizontal (*x*,*y*) direction. We thus fit the ADCP velocity observations (*u*,*v*) to the model

$$\begin{bmatrix} u_T(z,t) \\ v_T(z,t) \end{bmatrix} = \begin{bmatrix} a_x(z) \\ a_y(z) \end{bmatrix} \cdot \sin(\omega \cdot t) + \begin{bmatrix} b_x(z) \\ b_y(z) \end{bmatrix} \cdot \cos(\omega \cdot t) \qquad \text{(A1)}$$

using the method of least squares. The approach is strictly equivalent to the standard harmonic analysis of moored records and error estimation techniques are readily available, e.g., Münchow et al. (1992b). Formally, the uncertainty in estimated parameters depends upon the signal-to-noise-ratio

$$\text{SNR} = \sigma_{\text{signal}}/\sigma_{\text{residual}} = \pi * S_0/\varepsilon \qquad \text{(A2)}$$

where σ indicates a standard deviation, S_0 the amplitude of a sinusoidal signal, and ε the root-mean-square (rms) of the residuals. We thus find confidence limits for the tidal amplitude δS_0 as

$$\delta S_0 = 1.96 * \text{Var}(S_0)^{1/2} = 1.96 * (S_0/\text{SNR}) = 1.96 * \varepsilon/\pi \qquad \text{(A3)}$$

The factor of 1.96 refers to the 95% level of confidence (Münchow et al., 1992a). **Figure A1** shows all ellipse parameters along with 95% confidence limits for the semi-major axes

Semi-diurnal tidal currents of about 9.5 ±2.7cm/s occur within the pycnocline at 68-m depth. At 20-m depth amplitudes reduce to 6.5±2.2 cm/s while they become negligible (1.8±1.2 cm/s) at 228-m depth (Figure A1a). Tidal currents generally rotate clockwise around an ellipse that has a ratio between semi-minor and semi-major axes of about 0.5 (Figure A1b). The orientation of the semi-major axis varies smoothly from east-west near the surface to more north-south with depth and thus indicates counter-clockwise veering

with depth (Figure A1c). The phase angle changes little above 150-m depth, i.e., tidal currents above this depth are almost in-phase.

These results compare favorably with those reported by Sverdrup (1926) from mooring records of similar length, however, there is little physical reason to expect tidal currents in our study area to compare with tidal currents more than 200 km onshore. The agreement of our 1993 measurements over the slope with Sverdrup's 1923 measurements on the shelf is likely fortuitous. The neglected diurnal tidal currents contribute little to the tidal variance: Kowalik and Proshutinsky (1993) predict diurnal currents to reach about 1.4 cm/s 100 km to the west of our study area using a numerical model of the barotropic tides in the Arctic Ocean.

9.2 Tidal currents over the Chukchi slope

Tidal currents (u_T,v_T) to the east (Figure 1c) are modeled as

$$\begin{bmatrix} u_T(x, y, z, t) \\ v_T(x, y, z, t) \end{bmatrix} = \sum_{i=1}^{M} \sum_{k=1}^{K} \left(\begin{bmatrix} a_{i,k,x} \\ a_{i,k,y} \end{bmatrix} \cdot \sin(\omega_i \cdot t) + \begin{bmatrix} b_{i,k,x} \\ b_{i,k,y} \end{bmatrix} \cdot \cos(\omega_i \cdot t) \right) \phi_{i,k} \qquad \text{(A4)}$$

where $a_{i,k}$ and $b_{i,k}$ are constant coefficients and $\phi_{i,k}$ are biharmonic splines in three dimensions, i.e.,

$$\phi_{i,k} = \phi_{i,k}(x, y, z, x_{i,k}, y_{i,k}, z_{i,k}) = \sqrt{(x - x_{i,k})^2 + (y - y_{i,k})^2 + (z - z_{i,k})^2} \qquad \text{(A5)}$$

where (x,y,z) represent longitude, latitude, and depth that are non-dimensionalized by a horizontal length scale (133 km) and the local water depth. The scaling ensures that the spatial co-ordinates vary in the interval [0,1]. The fit depends strongly on $x_{i,k}$, $y_{i,k}$, and $z_{i,k}$ which are locations of K=3 specified nodes (Sandwell, 1987; Münchow, 2000) for M tidal

constituents whose locations must be chosen *a priori*. Note that no time-invariant or "mean" current is included in the fit. The approach here combines time-domain harmonic analysis with spatial interpolation methods (McIntosh, 1991.

Error estimation schemes are non-standard and we thus uses artificial signals embedded in prescribed noise, e.g.,

$$u(x, y, z, t) = 10 \cdot (y + 1 - z) \cdot \{\cos(\omega_{M_2} \cdot t) + 0.5 \cdot \sin(\omega_{K_1} \cdot t)\} + N(0, 5) \qquad \text{(A6)}$$

$$v(x, y, z, t) = N(0, 5) \qquad \text{(A7)}$$

The artificial data consist of semi-diurnal and diurnal signals at frequencies ω_{M_2} and ω_{K_1} and a Gaussian noise component N(0,5) with zero mean and a standard deviation of 5 cm/s; signal to noise ratios are O(1). **Figure A2** shows simulated currents. Using K=3 nodal locations, we find that fitting a single semi-diurnal constituent results in an absolute prediction error that is always smaller than 4 cm/s. The rms error is about 1.1 cm/s (Figure A2b). In contrast, absolute prediction errors reach 10 cm/s if we fit both semi-diurnal and diurnal constituents to our data. The rms error is about 3.2 cm/s. Note that the fit does not describe the tidal currents physically, but it reduces the tidal bias statistically.

Using K=3 and M=1, we show in **Figure A3** both raw and estimated tidal velocities as a function of time. The ship steams first along (t<24 hrs) and then across the upper slope (t>24 hrs). Measured currents are generally less than 20 cm/s, however, vertical current differences can exceed 30 cm/s as it does towards the end of the record (Figure A3b). The fitted tidal currents reach about 10 cm/s and their vertical variability is small. In summary, semi-diurnal tidal currents on the upper Chukchi slope appear largely barotropic, in phase, and, we speculate, result from frictional dynamics at tidal time scales.

10. References

Aagaard, K., 1988: A synthesis of the Arctic Ocean circulation. Rapp. P.-V. Reun. Cons. Int. Explor. Mer, 188, 11-22.

Aagaard, K., 1984: The Beaufort undercurrent. The Alaskan Beaufort Sea, P.W. Barnes and Coeditors, Academic Press, 47-71.

Aagaard, K., L.K. Coachman, and E.C. Carmack, 1981: On the halocline of the Arctic Ocean. Deep-Sea Res., 28A, 529-545.

Candela, J., R.C. Beardsley, and R. Limeburner, 1992: Separation of tidal and subtidal currents in ship-mounted acoustic Doppler current profilers. J. Geophys. Res., 97, 769-788.

Carmack, E.C., R.W. Macdonald, R.G. Perkin, F.A. McLaughlin, and R.J. Pearson, 1995: Evidence for warming of Atlantic water in the southern Canadian Basin of the Arctic Ocean: Results from the Larsen-93 expedition. Geophys. Res. Let., 22, 1061-1064.

Coachman, L.K. and K. Aagaard, 1988: Transports through Bering Strait: Annual and inter annual variability. J. Geophys. Res., 93, 15535-15539.

Coachman, L.K. and C.A. Barnes, 1963: The movement of Atlantic water in the Arctic Ocean. Arctic, 16, 9-16.

Coachman, L.K. and C.A. Barnes, 1961: The contribution of Bering Sea water to the Arctic Ocean. Arctic, 14, 145-161.

Collins, C.A., N. Garfield, R.G. Paquette, and E. Carter, 1996: Lagrangian measurements of subsurface poleward flow between 38N and 43N along the West Coast of the United States during summer, 1993. Geophys. Res. Let., 23, 2461-2464.

D'Asaro, E.A., 1988a: Observations of small eddies in the Beaufort Sea. J. Geophys. Res., 93, 6669-6684.

D'Asaro, E.A., 1988b: Generation of sub mesoscale eddies: A new mechanism. J. Geophys. Res., 93, 6685-6693.

Fonseca, T.R., 1989: An overview of the poleward undercurrent and upwelling along the Chilean coast. In: Neshyba, S.J., C.N.K. Mooers, R.L. Smith, and R.T. Barber (Eds.), "Poleward flows along eastern ocean boundaries," 203-218, Springer-Verlag, New York, NY.

Francis, J.A., A. Münchow, and R. Cermak, 1999: Analyses of long-term 10-m winds over the Arctic Basin. 5th Amer. Met. Soc. Conf. Polar Met. Oceanogr., Dallas, TX.

Huthnance, J.M., 1995: Circulation, exchange and water masses at the ocean margin: The role of physical processes at the shelf edge. Prog. Oceanogr., 35, 353-431.

Huthnance, J.M., 1992: Extensive slope currents and the ocean shelf boundary. Prog. Oceanogr., 29, 161-196.

Huffort, G.L., 1973: Warm water advection in the southern Beaufort Sea August-September 1971. J. Geophys. Res., 78, 2702-2707.

Huyer, A., P.M. Kosro, S.J. Lentz, and R.C. Beardsley, 1989: Poleward flow in the California Current system. In: Neshyba, S.J., C.N.K. Mooers, R.L. Smith, and R.T. Barber (Eds.), "Poleward flows along eastern ocean boundaries," 142-156, Springer-Verlag, New York, NY.

Jones,E.P., L.G. Anderson, and J.H. Swift, 1998: Distribution of Atlantic and Pacific waters in the upper Arctic Ocean: Implications for circulation. Geophys. Res. Let., 25, 765-768.

Klinger, B.A., 1994: Baroclinic eddy generation at a sharp corner in a rotating system. J. Geophys. Res., 99, 12515-12531.

Kowalik, Z. and A.Y. Proshutinsky, 1994: The Arctic Ocean tides. The Polar Oceans and Their Role in Shaping the Global Environment, O.M. Johannessen and Coeditors, Amer. Geophys. Union, 137-158.

Kowalik, Z. and A.Y. Proshutinsky, 1993: Diurnal tides in the Arctic Ocean. J. Geophys. Res., 98, 16449-16468.

Macdonald, R., 1996: Awakenings in the Arctic. Nature, 380, 286-287.

Manley, T.O. and K. Hunkins, 1985: Mesoscale eddies in the Arctic Ocean. J. Geophys. Res., 90, 4911-4930.

McIntosh, P.C., 1991: Oceanographic data interpolation: Objective analysis and splines. J. Geophys. Res., 95, 13529-13541.

McLaughlin, F.A., E.C. Carmack, R.W. Macdonald, and J.K.B. Bishop, 1996: Physical and geochemical properties across the Atlantic/Pacific water mass front in the southern Canadian Basin. J. Geophys. Res., 101, 1183-1197.

Mountain,D.G., L.K. Coachman, and K. Aagaard, 1976: On the flow through Barrow Canyon. J. Phys. Oceanogr., 6, 461-470.

Münchow, A., 2000: Detiding three-dimensional velocity survey data in coastal waters. J. Atmos. Ocean. Tech., in press.

Münchow, A., 1998: Tidal currents in a topographically complex channel. Cont. Shelf Res., 18. 561-584.

Münchow, A. and E.C. Carmack, 1997: Synoptic flow and density observations near an Arctic shelf break. J. Phys. Oceanogr., 27, 1402-1419.

Münchow, A., C.S. Coughran, M.C. Hendershott, and C.D. Winant, 1995: Performance and calibration of a subsurface towed acoustic Doppler current profiler. J. Atmos. Ocean. Tech., 12, 435-444.

Münchow, A., A.K. Masse, and R.W. Garvine, 1992a: Astronomical and nonlinear tidal currents in a coupled estuary shelf system. Cont. Shelf Res., 12, 471-498.

Münchow, A., R.W. Garvine, and T.F. Pfeiffer, 1992b: Subtidal currents from a shipboard acoustic Doppler current profiler in tidally dominated waters. Cont. Shelf Res., 12, 499-515.

Newton, J.L., K. Aagaard, and L.K. Coachman, 1975: Baroclinic eddies in the Arctic Ocean. Deep-Sea Res., 21, 707-719.

Paquette, R.G. and R.H. Bourke, 1974: Observations on the coastal current of Arctic Alaska. J. Mar. Res., 32, 195-207.

Pedlosky, J., 1986: Geophysical Fluid Dynamics. 2nd ed., Springer Verlag, New York, NY.

Plueddemann, A.J., R. Krishfield, T. Takizawa, K. Hatakeyama, and S. Honjo, 1998: Upper ocean velocities in the Beaufort gyre. Geophys. Res. Let., 25, 183-186.

Quadfasel, D., A. Sy, and B. Rudels, 1993: A ship of opportunity section to the North Pole: upper ocean temperature observations. Deep-Sea Res., 40, 777-789.

Sandwell, D.T., 1987: Biharmonic spline interpolation of GEOS-3 and SEASAT altimeter data. Geophys. Res. Let., 23, 2101-2104.

Signorini, S.R., A. Münchow, and D. Haidvogel, 1997: Flow dynamics of a wide Arctic canyon. J. Geophys. Res., 102, 18661-18680.

Smith, J.N, K.M. Ellis, and T. Boyd, 1999: Circulation in the central Arctic Ocean revealed by nuclear fuel reprocessing tracers from scientific ice expeditions 1995 and 1996. J. Geophys. Res., 104, 29663-29677.

Stern, M.E, and J.A. Whitehead, 1990: Separation of a boundary jet in a rotating fluid. J. Fluid. Mech., 217, 41-69.

Stigebrandt, A., 1984: The North Pacific: A global scale estuary. J. Phys. Oceanogr., 14, 464-470.

Sverdrup, H.U., 1926: The tides on the North Siberian shelf: Their bearing on the existence of land in the Arctic Sea and their dynamics. J. Wash. Aca. Sci., 16, 529-540.

Sverdrup, H.U., 1929: The waters on the North-Siberian shelf. The Norwegian North Polar Expedition with the “Maud”, 1918-1925. Scientific Results, 4(2), Bergen, Norway.

Treshnikov, A.F., 1977: Water masses of the Arctic basin. In: Dunbar, M. (Ed.), “Polar Oceans”, 17-31, Arctic Inst. North Am. Calgary, Alberta, Canada.

Yankovsky, A.E. and D.C. Chapman, 1997: Anticyclonic eddies trapped on the continental shelf by topographic irregularities. J. Geophys. Res., 102, 5625-5639.

11. Figure captions

Figure 1. Maps of the study area: (A) Large-scale view of study area with geographic features. Sections labeled C, D, and E follow the notation of McLaughlin (1996). Symbols indicate select 1993 (triangles) and 1923 (circles) stations (numbers indicate mooring labels used in Sverdrup, 1929). Also shown are the 50-m, 100-m, 1000-m, and 2000-m isobaths. Note the broad shelves and slopes of the East Siberian and Chukchi Seas as compared to the narrow shelf and slope region of the Beaufort Sea. The focus of the present study is (B) the triangular area between the 300-m and 800-m isobath and (C) area C between the 100-m and 300-m isobath. Station names from the "Triangle" begin with a "T" and TA, TB, and TC refer to the corners. Data from the highlighted stations are shown in Figure 3. Maps B and C have the same scale with bottom contour intervals of 100-m. Note the much steeper slope in (B) as compared with (C).

Figure 2. Comparison of the ship's absolute velocity over ground as determined from navigational data (GPS) and bottom tracking (BT) ADCP data after calibration according to Münchow et al. (1995). The ADCP was towed from the *CCGS Henry Larsen* on 11-12 September 1993 and 21-23 September 1993 in areas D and C, respectively (see Figure 1 for locations). The solid line indicates the perfect fit.

Figure 3. Temperature vs. salinity diagram for the upper 500-m of the water column at select stations (see Figures 1 and 5 for locations). Contours are density anomalies. Symbols indicate observations at 2-m vertical intervals. The circled density labels indicate the isopycnals for which property maps are shown in Figure 4. Note the scatter of the data from the "Triangle" area between the upper and lower halocline waters.

Figure 4. Properties on density surfaces σ_θ=26.3 (top panels A and B), σ_θ=27.5 (middle panels C and D) and σ_θ=27.9 (bottom panels E and F) representing the upper and lower halocline as well as Atlantic core waters, respectively. Shown are the potential temperature θ (left panels A, C, and E) and pressure p (right panels B, D, and F). Symbols indicate station locations. Note the large temperature gradients in the area termed “triangle” in panel (D) for the lower halocline and in the area near the “Mendeleyev Ridge” in panel E for the Atlantic core waters. These regions indicate water mass boundaries separating Eastern Arctic from Western Arctic assemblies that McLaughlin et al. (1996) described using data from three stations circled in panel (A).

Figure 5. Across-shore sections (see Figure 1 for locations) of density anomaly σ_θ for sections across the slope of (A) the East Siberian Sea into the Makarov Basin, (B) the western Chukchi Sea into the Chukchi Abyssal Plain, and (C) the eastern Chukchi Sea into the Canada Basin. Dotted lines indicate location of CTD casts. The surface layer (σ_θ<26.2) is not shown for clarity. Note the sharp and sloping interface in (C) that contrasts with the broad spread of the same isopycnals in (A).

Figure 6. Vertical profiles of velocity vectors from the ADCP survey around the triangle (see Figure 1 for locations). The vertical and error velocity in the lower left and right panel are data quality indicators only. The large velocity and its vertical shear indicates an anti-cyclonic eddy in the south-eastern corner of the triangle (see also Figures 7 and 8).

Figure 7. Detided velocity vectors over contours of σ_θ at (A) 60-m, (B) 100-m, and (C) 140-m below the surface. Note the anti-cyclonic flow in the south-western corner of the triangle with a maximum at about 100-m depth.

Figure 8. Velocity components along the southern leg of the triangle at 75°N latitude. The symbols at 10-m depth indicate the location of vertical profiles from which the contours are drawn. Note the strong convergence in (A) and the anti-cyclonic lateral shear in (B) at about 50 to 100-m below the surface between 174°W and 173°W longitude. Both ice and seabirds accumulated at this location.

Figure 9. Thermal wind diagnostics along the sides of the triangle from TB (-50 km) to TC (0 km) and to TA (50 km): (A) Potential density, (B) thermal wind velocity in cm/s, and (C) a comparison of thermal wind velocity at 90-m (line) with observed ADCP velocities at 92-m (symbols). The thermal wind velocities are relative to no flow at -275-m depth and are perpendicular to the section with positive velocities having a westward flow component, however, note that both legs of the triangle are shown, e.g, a positive flow between TC and TA is into the triangle while it is out of the triangle between TB and TC.

Figure 10. Detided velocity vectors over the upper slope of the Chukchi Sea at (A) 68-m, (B) 100-m, and (C) 140-m depth. Note the flow reversal at depth. The ship's steaming direction and time at two locations is indicated in (A). Contours are bottom topography from ETOPO5 that do not always agree with those measured by the ADCP along the ship track.

Figure 11. Detided velocity section across the upper slope of the Chukchi Sea for (A) along-shore and (B) across-shore components. The symbols near 10-m depth indicate the location of ADCP velocity profiles. The profiling of this section took about 7 hours on 23 September, 1993.

Figure A1. M_2 tidal ellipse parameters from the ADCP survey around the triangle (see Figure 1 for location): (A) amplitude of the semi-major axis (RMAJ), (B) amplitude of the semi-minor axis (RMIN), (C) orientation of the semi-major axis counter-clockwise from true East (ORIE), and (D) phase angle (PHASE). Negative amplitudes of the semi-minor axis RMIN indicate clockwise rotation of currents around the tidal ellipse. The dashed curves in (A) and (B) represent estimates of 95% confidence limits.

Figure A2. Tidal prediction error from artificial data: (a) Symbols represent artificial signal and noise at measurement locations while the solid curves show the artificial tidal signal at y=0.5 at three depth levels, z/H=1 represents the bottom; (b) prediction errors fitting only a semi-diurnal constituent at K=3 three nodes (rms=1.1 cm/s); and (c) prediction errors fitting both semi-diurnal and diurnal constituent at K=3 nodes (rms=3.2 cm/s).

Figure A3. Raw (small symbols) and tidal (large symbols) currents along (t<24) and across (t>24) the western Chukchi shelf as a function of time t in hours after Sept. 22, 1993 0:00 UTC of (A) eastward and (B) northward components; (C) shows the depth of the bottom. The gaps reflect either poor data or stations time when the ship moved or drifted at less than 3 kn. The scatter for both raw and tidal data represents vertical current shear, i.e., data from all depths are shown. A single semi-diurnal constituent for K=3 nodes is used to estimate the tidal currents shown.

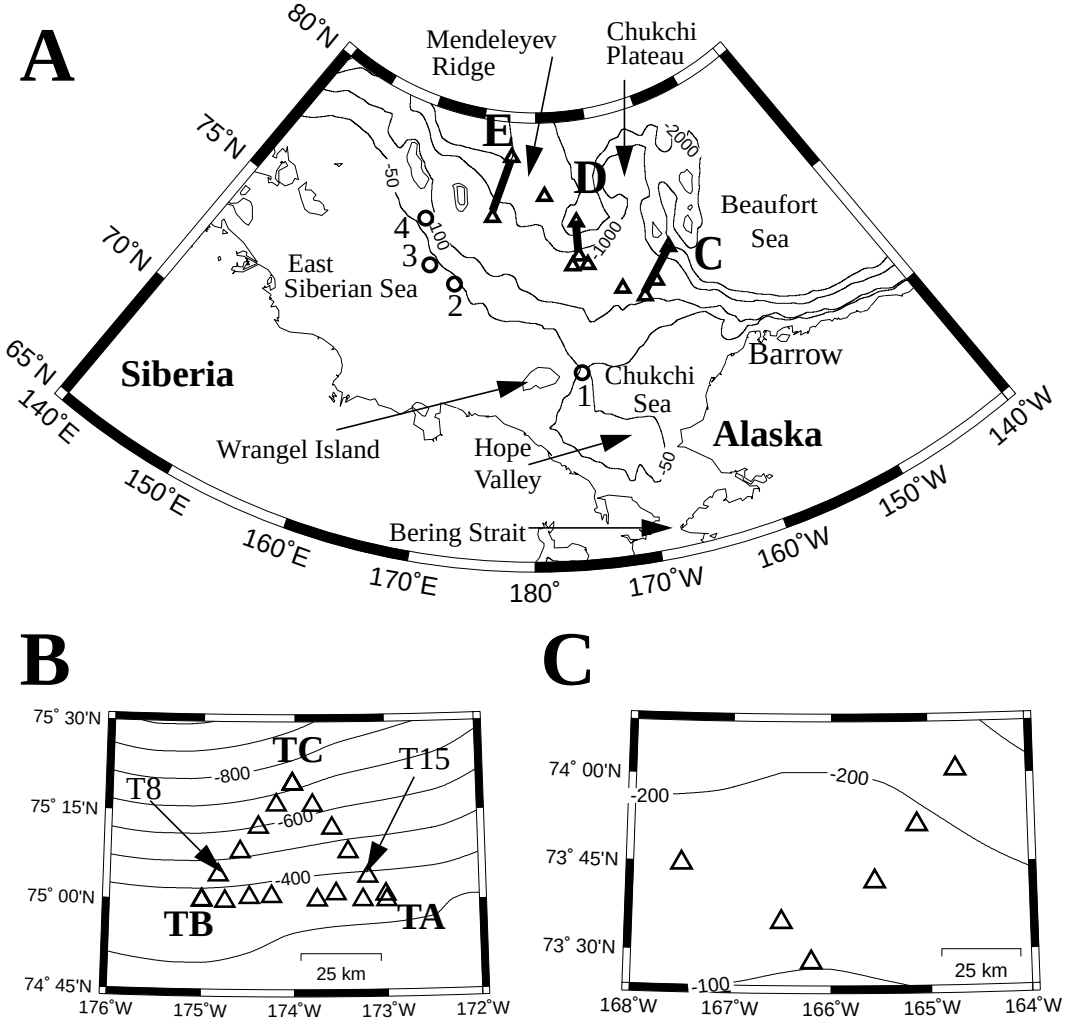

FIGURE 1. Maps of the study area: (A) Large-scale view of study area with geographic features. Sections labeled C, D, and E follow the notation of McLaughlin (1996). Symbols indicate select 1993 (triangles) and 1923 (circles) stations (numbers indicate mooring labels used in Sverdrup, 1929). Also shown are the 50-m, 100-m, 1000-m, and 2000-m isobaths. Note the broad shelves and slopes of the East Siberian and Chukchi Seas as compared to the narrow shelf and slope region of the Beaufort Sea. The focus of the present study is (B) the triangular area between the 300-m and 800-m isobath and (C) area C between the 100-m and 300-m isobath. Station names from the "Triangle" begin with a "T" and TA, TB, and TC refer to the corners. Data from the highlighted stations are shown in Figure 3. Maps B and C have the same scale with bottom contour intervals of 100-m. Note the much steeper slope in (B) as compared with (C).

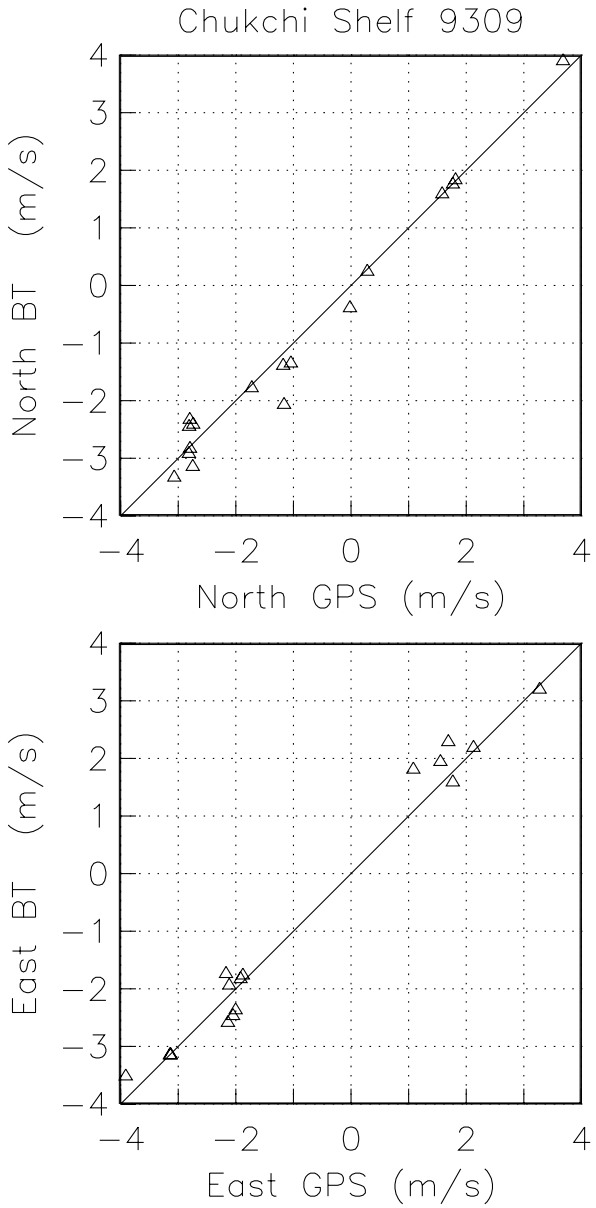

FIGURE 2. Comparison of the ship's absolute velocity over ground as determined from navigational data (GPS) and bottom tracking (BT) ADCP data after calibration according to Münchow et al. (1995). The ADCP was towed from the *CCGS Henry Larsen* on 11-12 September 1993 and 21-23 September 1993 in areas D and C, respectively (see Figure 1 for locations). The solid line indicates the perfect fit.

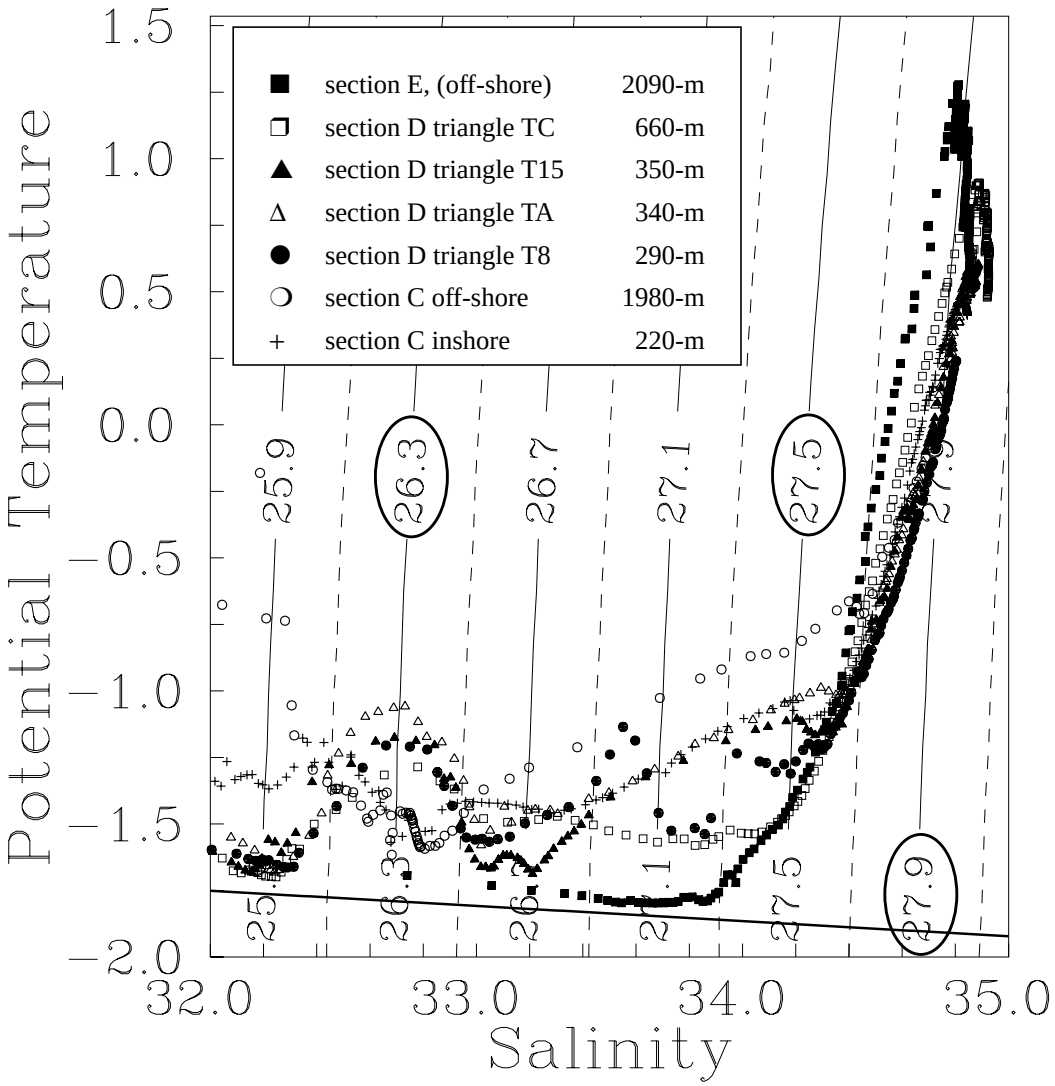

FIGURE 3. Temperature vs. salinity diagram for the upper 500-m of the water column at select stations (see Figures 1 and 5 for locations). Contours are density anomalies. Symbols indicate observations at 2-m vertical intervals. The circled density labels indicate the isopycnals for which property maps are shown in Figure 4. Note the scatter of the data from the “Triangle” area between the upper and lower halocline waters.

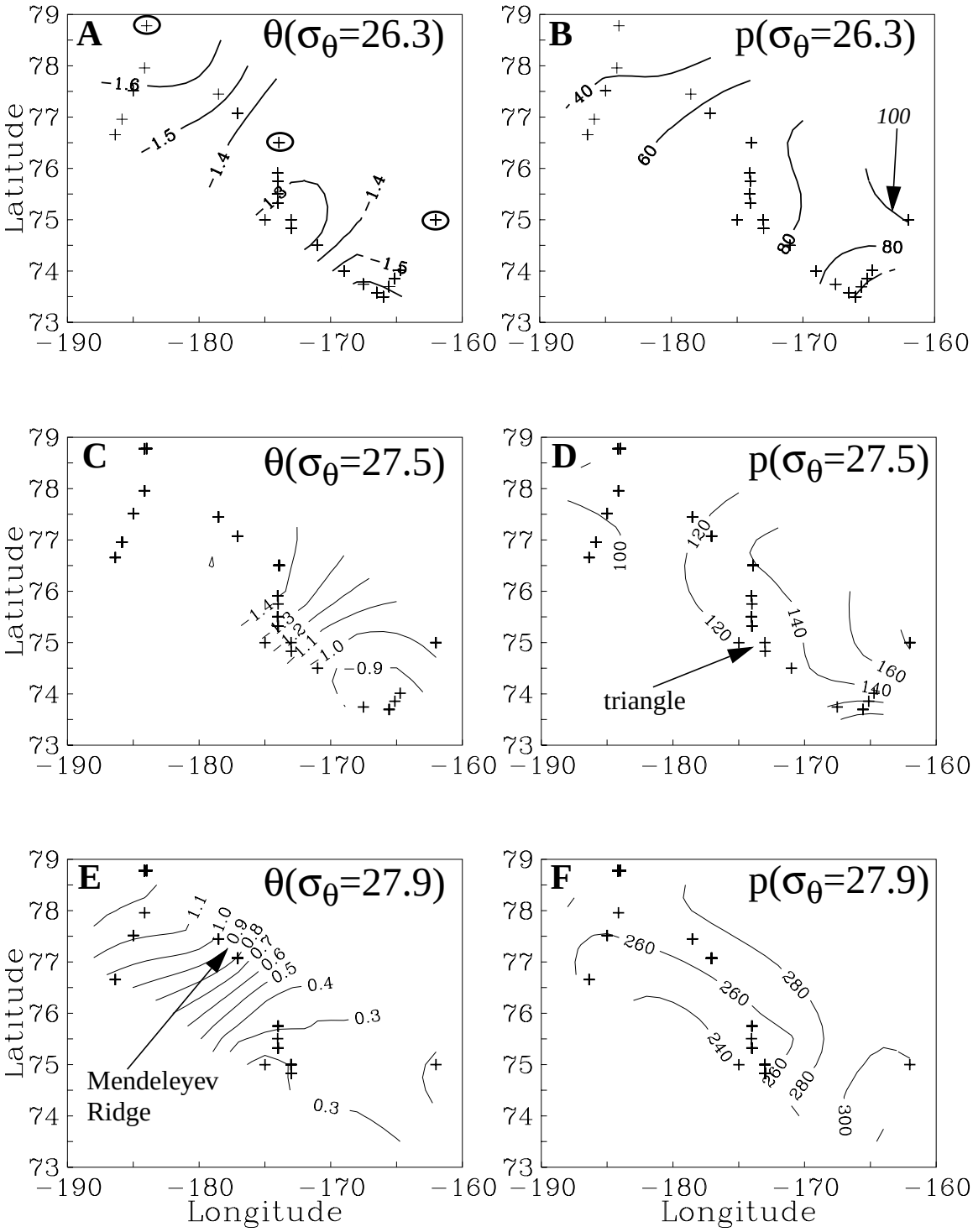

FIGURE 4. Properties on density surfaces σ_θ=26.3 (top panels A and B), σ_θ=27.5 (middle panels C and D) and σ_θ=27.9 (bottom panels E and F) representing the upper and lower halocline as well as Atlantic core waters, respectively. Shown are the potential temperature θ (left panels A, C, and E) and pressure p (right panels B, D, and F). Symbols indicate station locations. Note the large temperature gradients in the area termed "triangle" in panel (D) for the lower halocline and in the area near the "Mendeleyev Ridge" in panel E for the Atlantic core waters. These regions indicate water mass boundaries separating Eastern Arctic from Western Arctic assemblies that McLaughlin et al. (1996) described using data from three stations circled in panel (A).

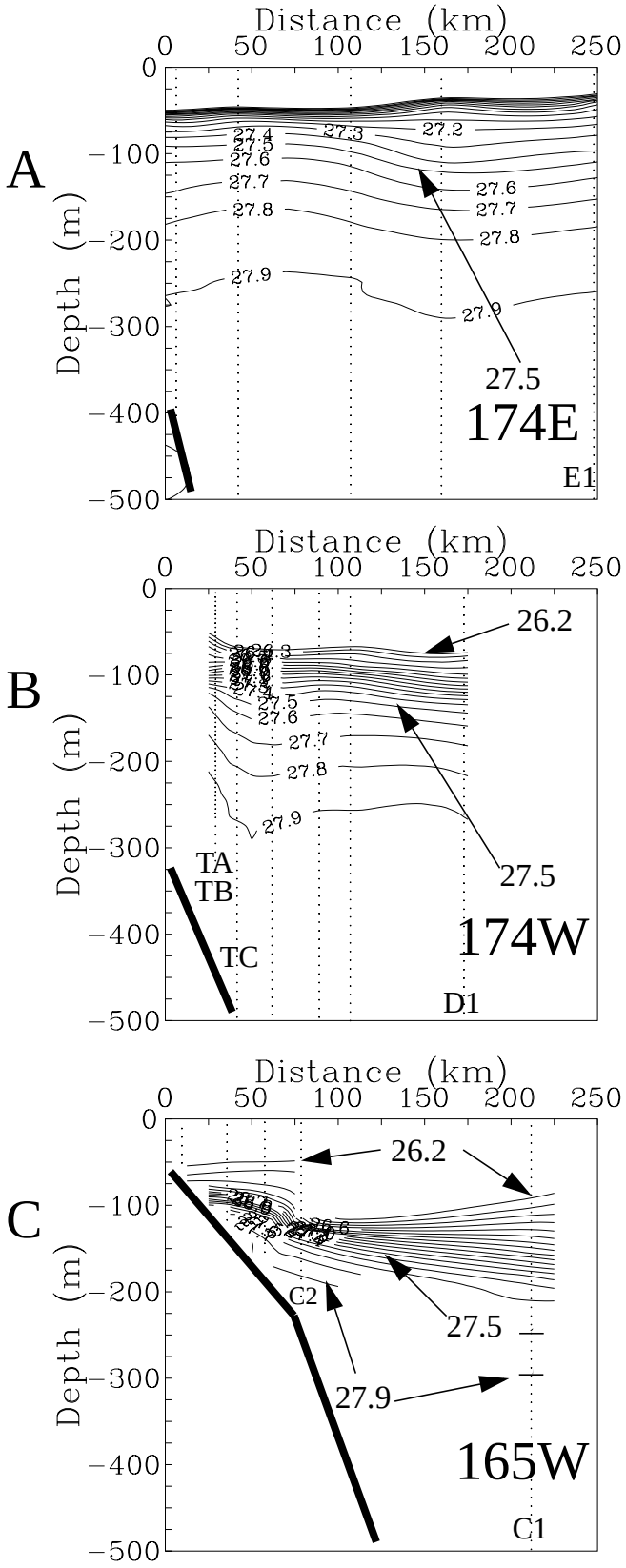

FIGURE 5. Across-shore sections (see Figure 1 for locations) of density anomaly σ_θ for sections across the slope of (A) the East Siberian Sea into the Makarov Basin, (B) the western Chukchi Sea into the Chukchi Abyssal Plain, and (C) the eastern Chukchi Sea into the Canada Basin. Dotted lines indicate location of CTD casts. The surface layer (σ_θ<26.2) is not shown for clarity. Note the sharp and sloping interface in (C) that contrasts with the broad spread of the same isopycnals in (A).

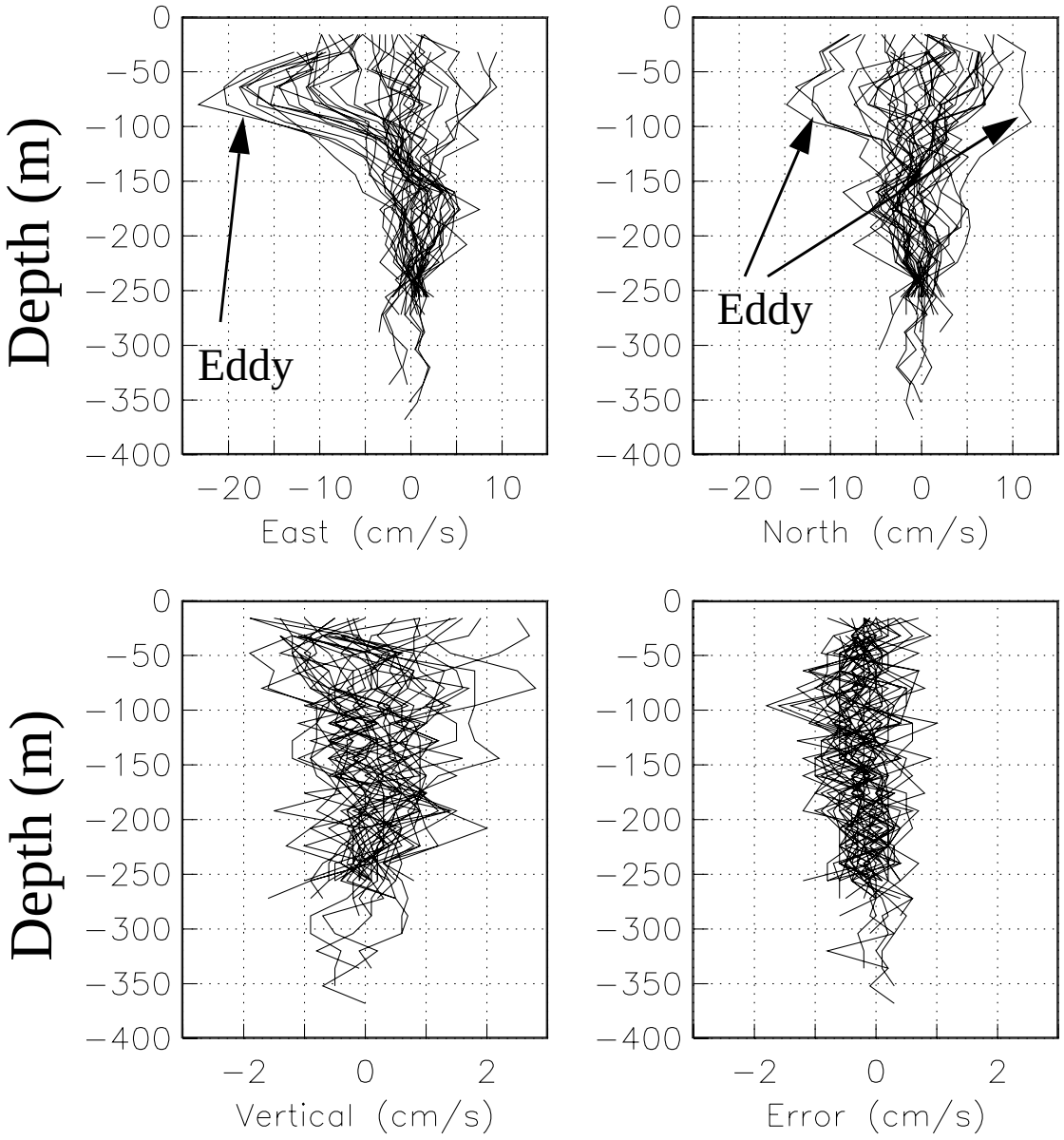

FIGURE 6. Vertical profiles of velocity vectors from the ADCP survey around the triangle (see Figure 1 for locations). The vertical and error velocity in the lower left and right panel are data quality indicators only. The large velocity and its vertical shear indicates an anti-cyclonic eddy in the south-eastern corner of the triangle (see also Figures 7 and 8).

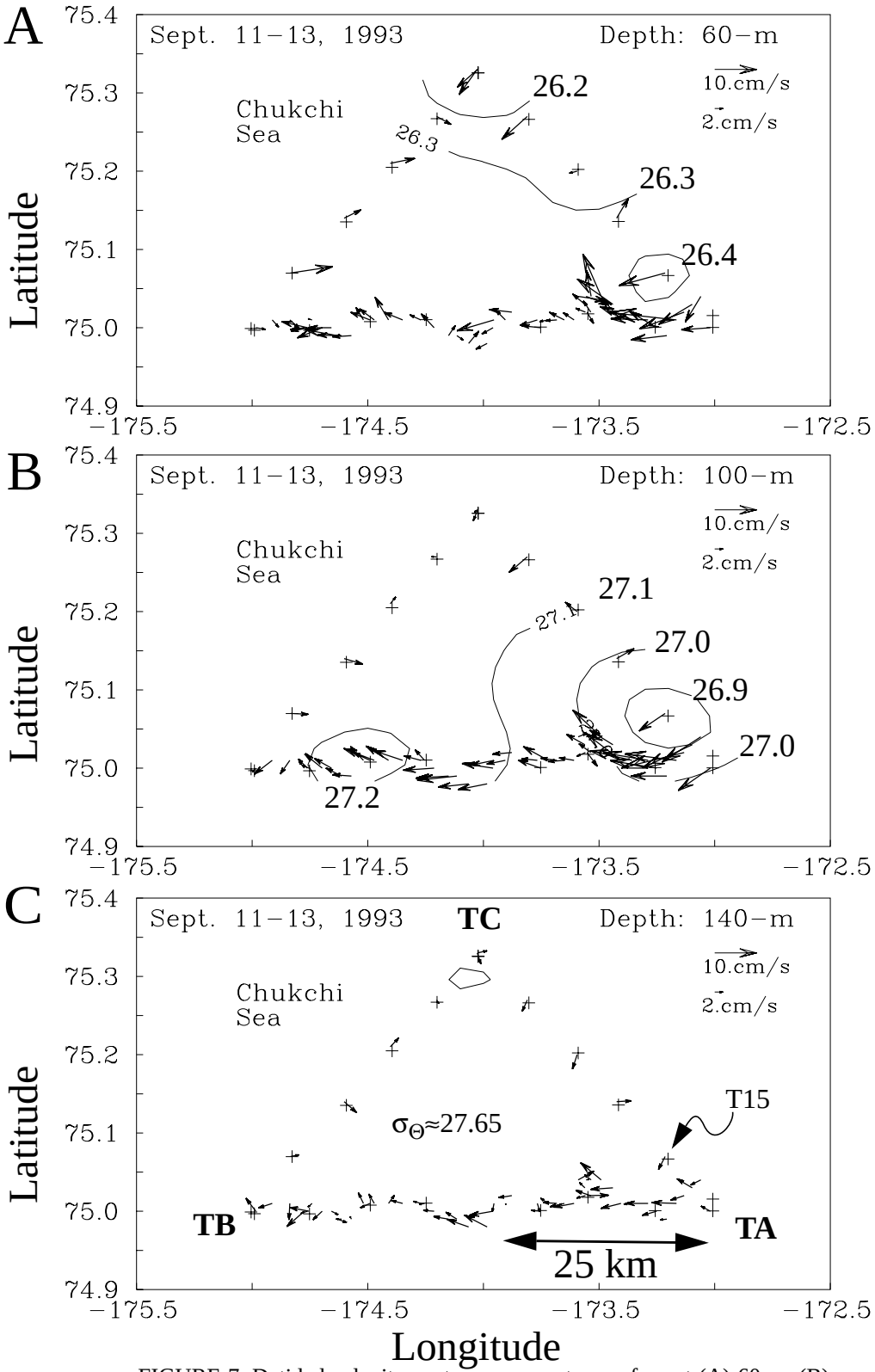

FIGURE 7. Detided velocity vectors over contours of σ_θ at (A) 60-m, (B) 100-m, and (C) 140-m below the surface. Note the anti-cyclonic flow in the south-western corner of the triangle with a maximum at about 100-m depth.

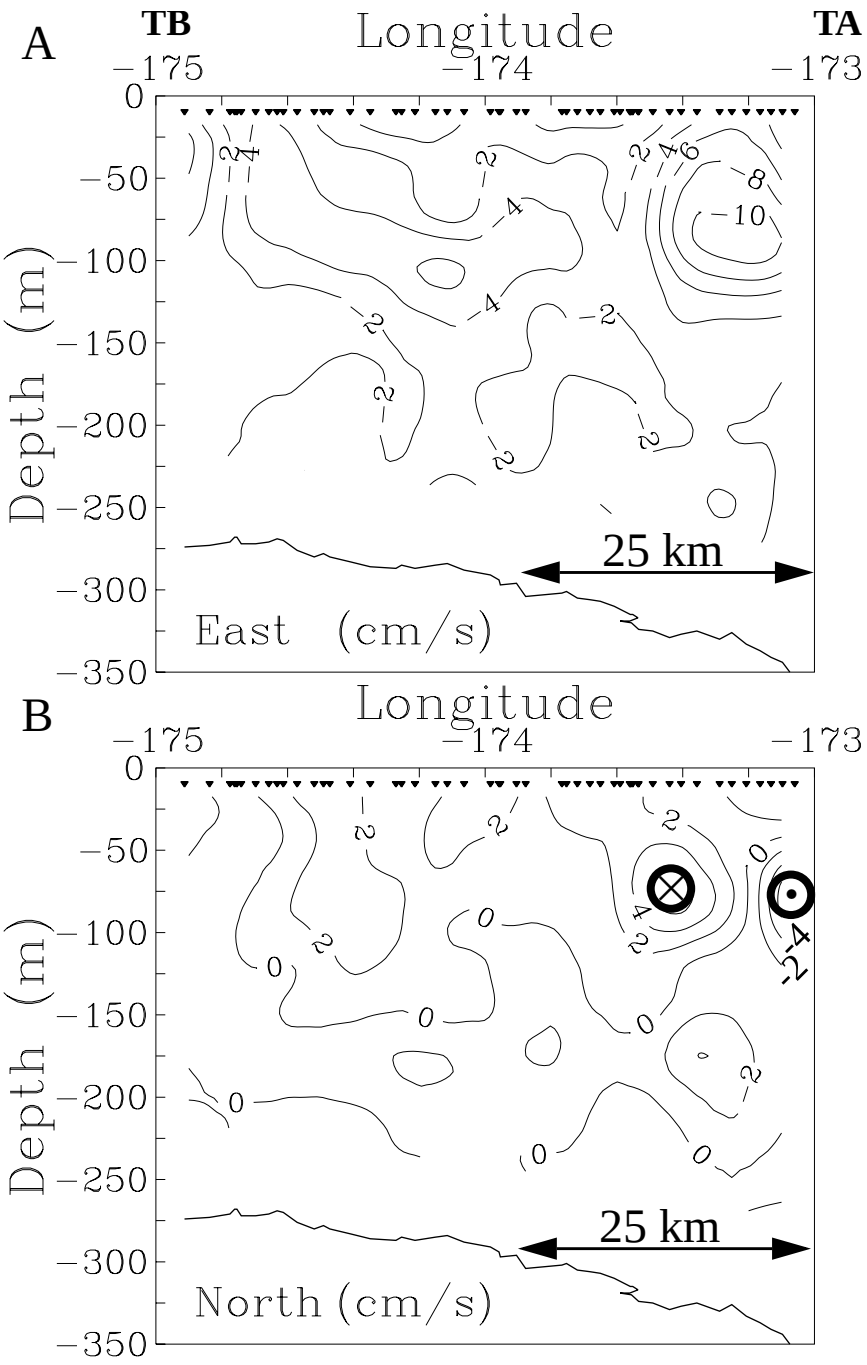

FIGURE 8. Velocity components along the southern leg of the triangle at 75°N latitude. The symbols at 10-m depth indicate the location of vertical profiles from which the contours are drawn. Note the strong convergence in (A) and the anti-cyclonic lateral shear in (B) at about 50 to 100-m below the surface between 174°W and 173°W longitude. Both ice and seabirds accumulated at this location.

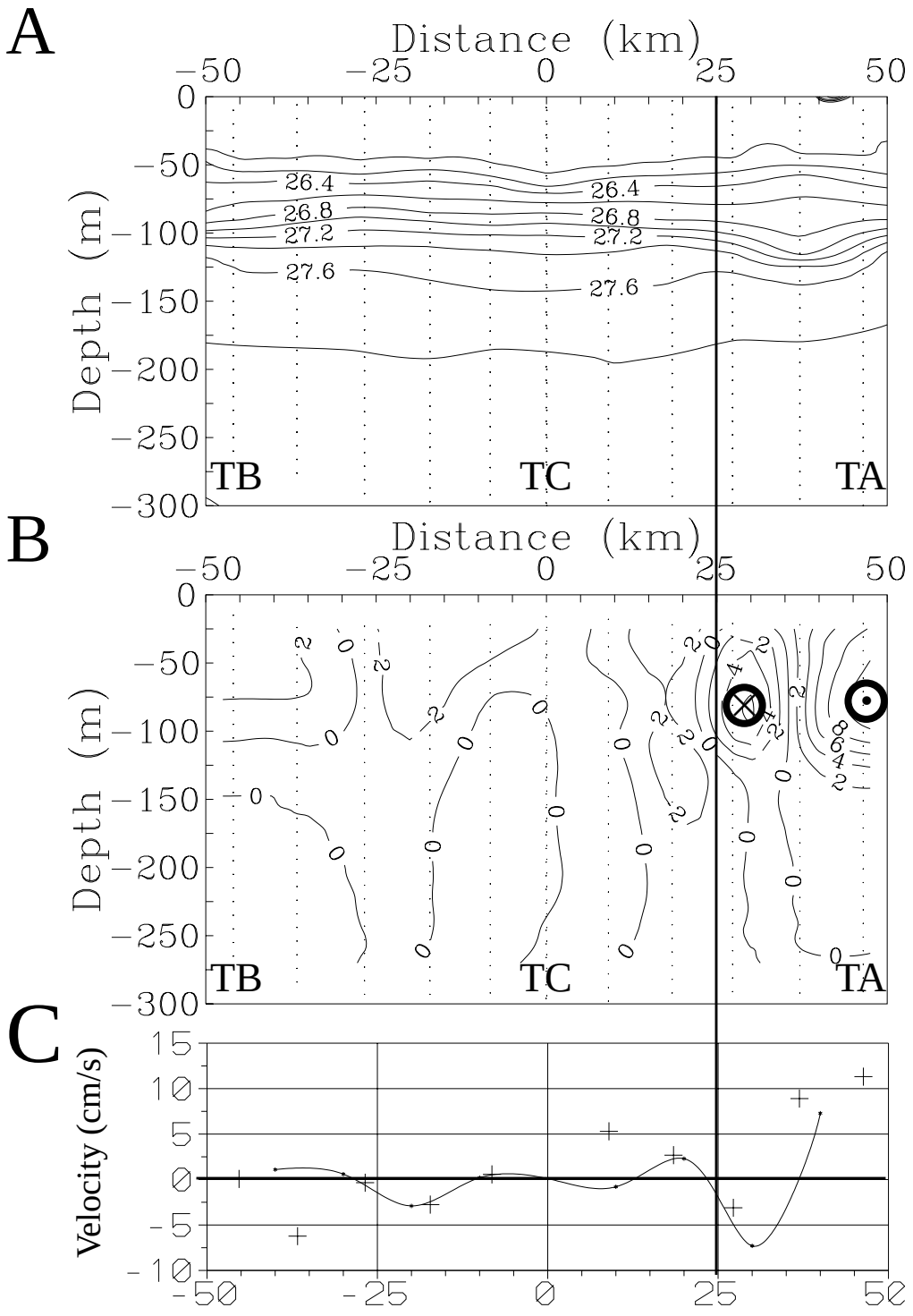

FIGURE 9. Thermal wind diagnostics along the sides of the triangle from TB (-50 km) to TC (0 km) and to TA (50 km): (A) Potential density, (B) thermal wind velocity in cm/s, and (C) a comparison of thermal wind velocity at 90-m (line) with observed ADCP velocities at 92-m (symbols). The thermal wind velocities are relative to no flow at -275-m depth and are perpendicular to the section with positive velocities having a westward flow component, however, note that both legs of the triangle are shown, e.g, a positive flow between TC and TA is into the triangle while it is out of the triangle between TB and TC.

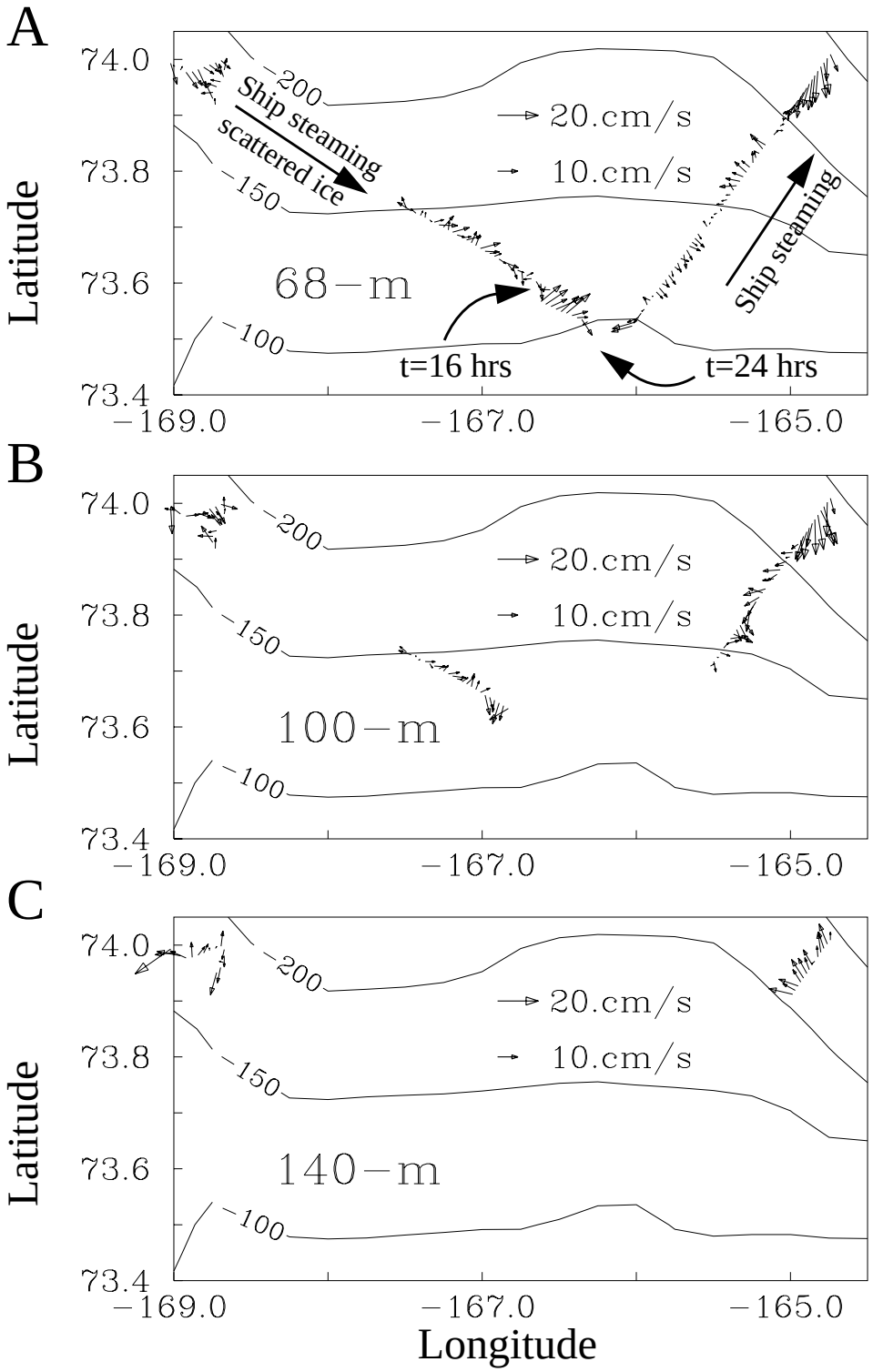

FIGURE 10. Detided velocity vectors over the upper slope of the Chukchi Sea at (A) 68-m, (B) 100-m, and (C) 140-m depth. Note the flow reversal at depth. The ship's steaming direction and time at two locations is indicated in (A). Contours are bottom topography from ETOPO5 that do not always agree with those measured by the ADCP along the ship track.

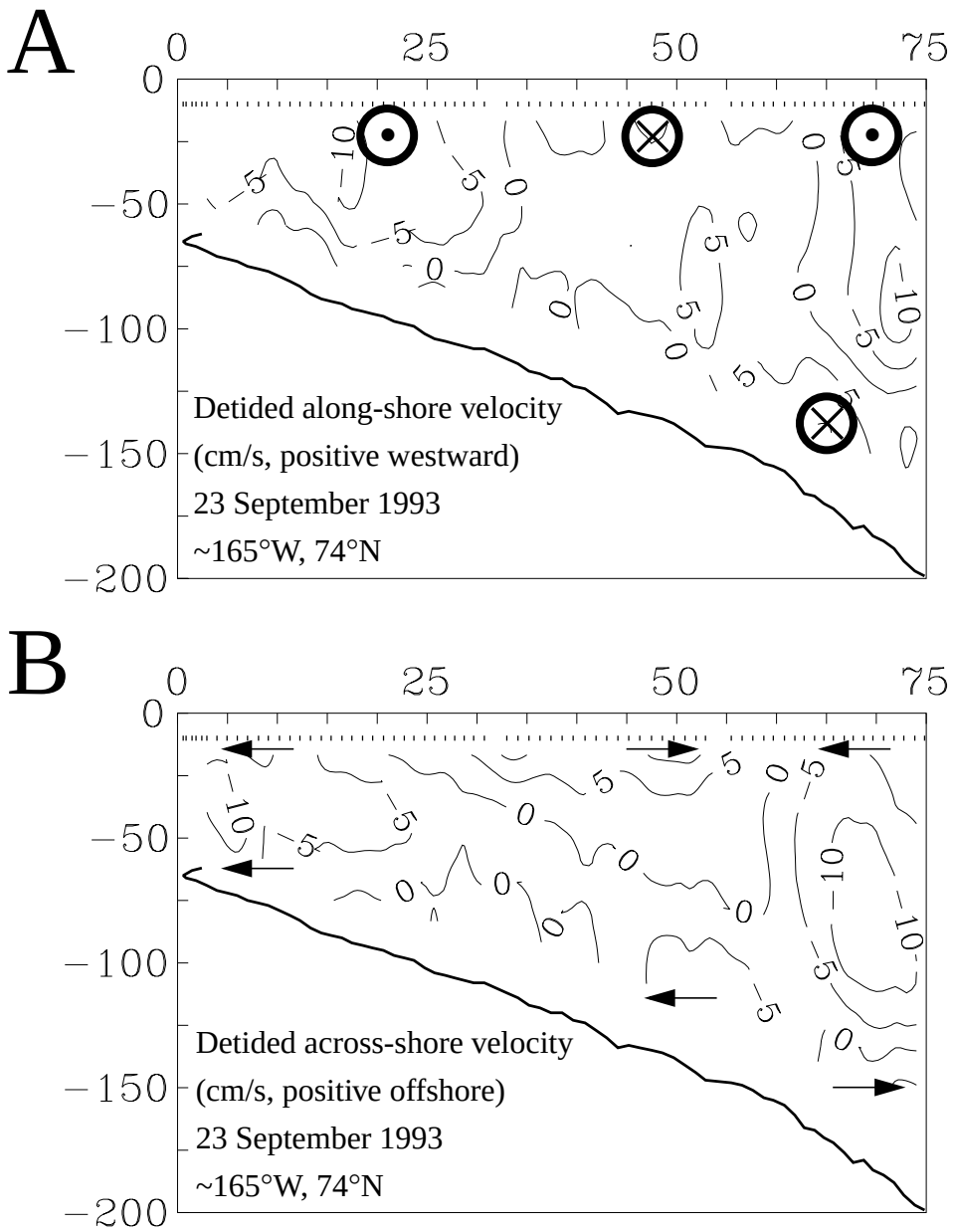

FIGURE 11. Detided velocity section across the upper slope of the Chukchi Sea for (A) along-shore and (B) across-shore components. The symbols near 10-m depth indicate the location of ADCP velocity profiles. The profiling of this section took about 7 hours on 23 September, 1993.

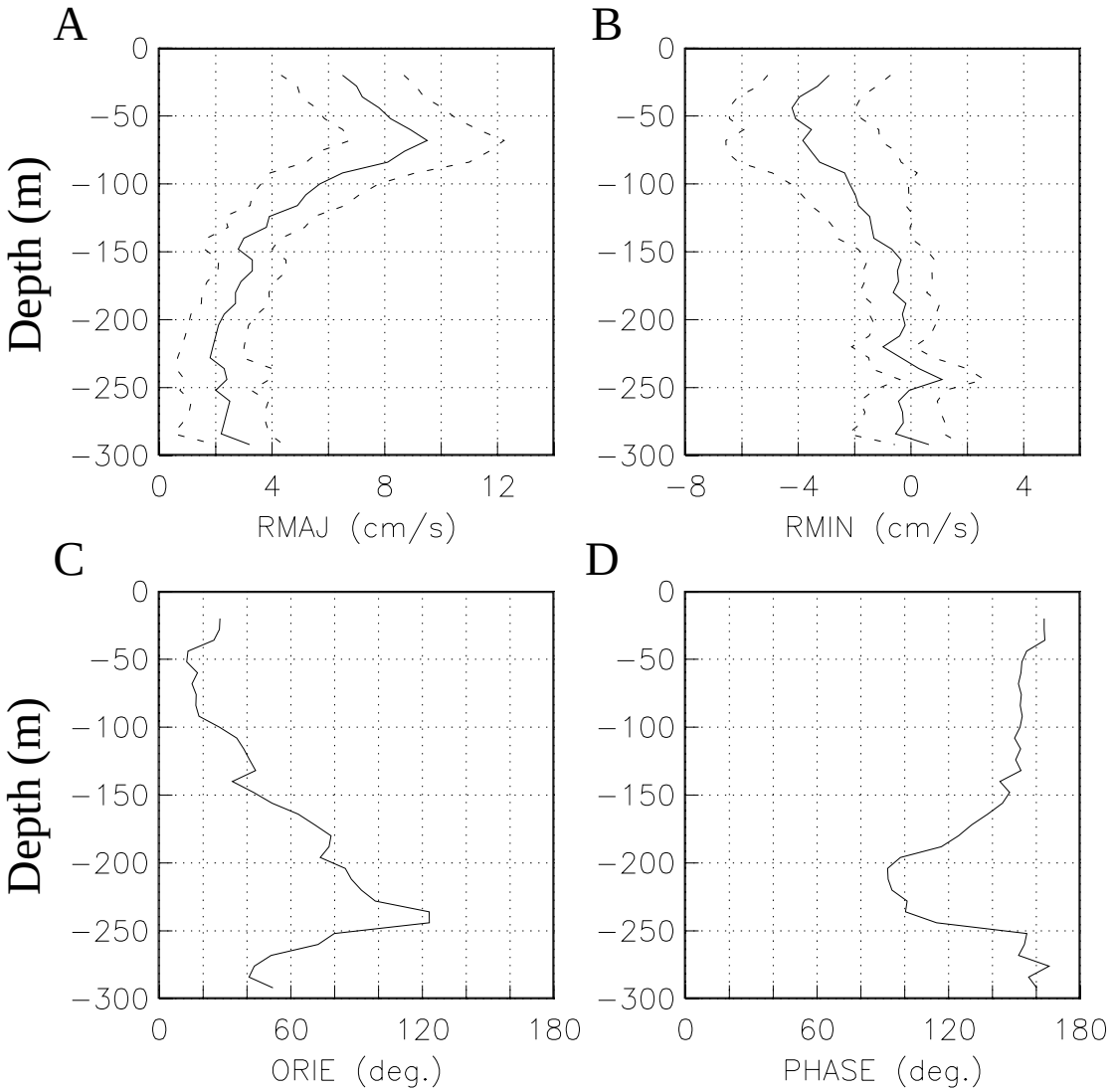

FIGURE A1. M_2 tidal ellipse parameters from the ADCP survey around the triangle (see Figure 1 for location): (A) amplitude of the semi-major axis (RMAJ), (B) amplitude of the semi-minor axis (RMIN), (C) orientation of the semi-major axis counter-clockwise from true East (ORIE), and (D) phase angle (PHASE). Negative amplitudes of the semi-minor axis RMIN indicate clockwise rotation of currents around the tidal ellipse. The dashed curves in (A) and (B) represent estimates of 95% confidence limits.

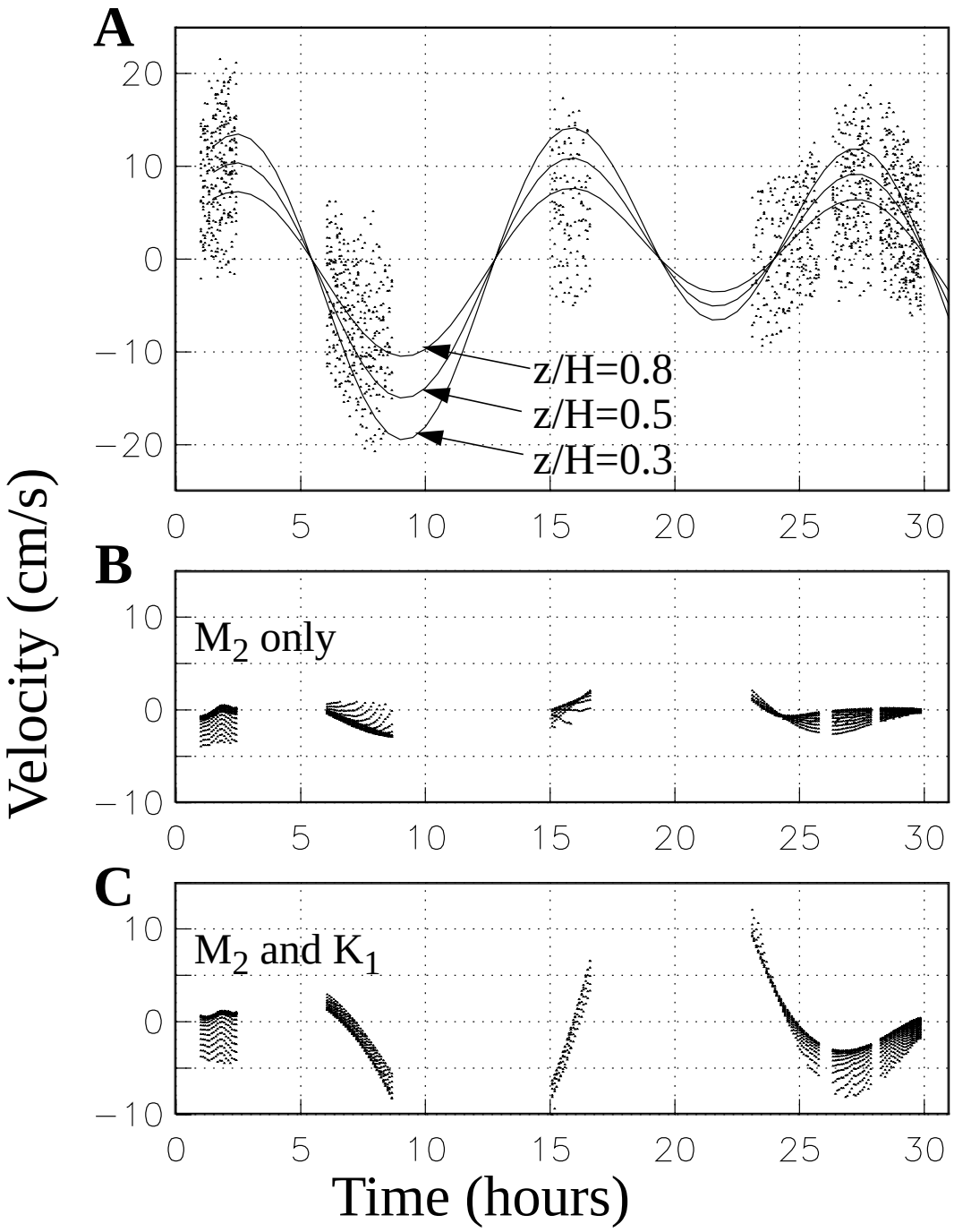

FIGURE A2. Tidal prediction error from artificial data: (a) Symbols represent artificial signal and noise at measurement locations while the solid curves show the artificial tidal signal at y=0.5 at three depth levels, z/H=1 represents the bottom; (b) prediction errors fitting only a semi-diurnal constituent at K=3 three nodes (rms=1.1 cm/s); and (c) prediction errors fitting both semi-diurnal and diurnal constituent at K=3 nodes (rms=3.2 cm/s).

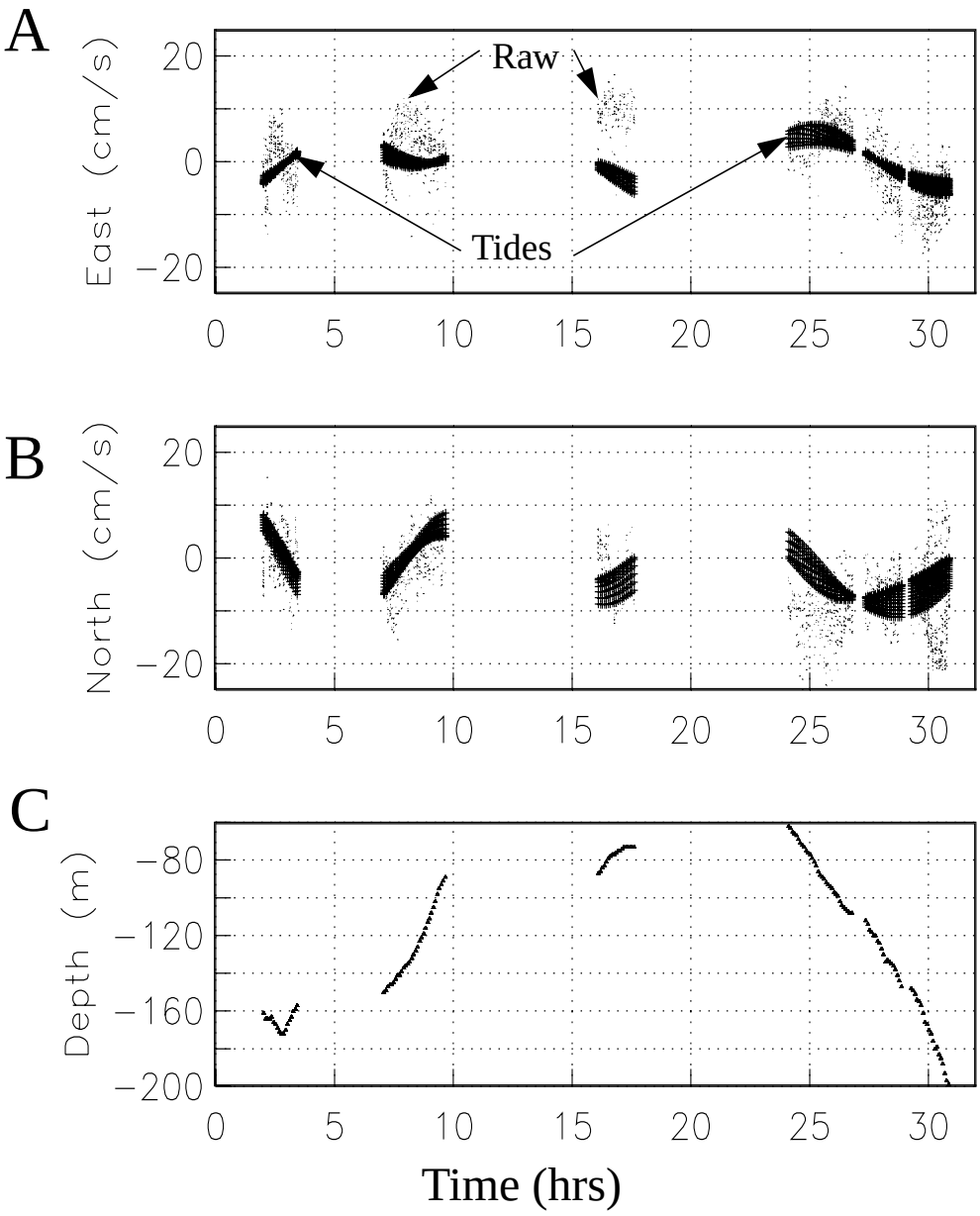

FIGURE A3. Raw (small symbols) and tidal (large symbols) currents along (t<24) and across (t>24) the western Chukchi shelf as a function of time t in hours after Sept. 22, 1993 0:00 UTC of (A) eastward and (B) northward components; (C) shows the depth of the bottom. The gaps reflect either poor data or stations time when the ship moved or drifted at less than 3 kn. The scatter for both raw and tidal data represents vertical current shear, i.e., data from all depths are shown. A single semi-diurnal constituent for K=3 nodes is used to estimate the tidal currents shown.